Stanford Exploration Project, Report 77, November 17, 1997, pages 1–20

Anti-aliased Kirchhoff 3-D migration: a salt intrusion example

David E. Lumley[1]

keywords: *three-dimensional, filtering, aliasing, algorithm, poststack, interpolation, faults*

ABSTRACT

Spatial aliasing of Kirchhoff migration imaging operators can seriously degrade the quality of subsurface reflectivity images. Sparse and/or irregular 3-D acquisition geometries can adversely magnify the problem in the presence of steep reflector dip. An anti-aliasing method is implemented to ameliorate Kirchhoff migration operator aliasing, based on local time and dip variant triangle filtering. The local anti-aliasing filters are efficiently applied as 3-point time filters after a step each of causal and acausal temporal trace integration. The anti-aliased migration is compared to a standard aperture-weighted Kirchhoff 3-D poststack time migration of a steep-dip salt intrusion from the Gulf of Mexico. Preliminary results indicate that the anti-aliased migration appears to enhance the resolution of steep salt-sediment interfaces and faults, compared to the standard migration. Both algorithms are implemented on the 32-node Connection Machine (CM5) at the Stanford Exploration Project.

INTRODUCTION

Spatial aliasing of Kirchhoff migration operators occurs when the migration summation surface slices through the input data volume at moveouts greater than the spatial and temporal dip Nyquist frequency. This operator aliasing can severely degrade the quality of the final subsurface image. The aliasing can become worse for 3-D surveys since crossline trace spacings are often at least twice as long as inline spacings. Additionally, scattered energy from steep-dip reflectors, such as faults and salt flanks, magnifies the aliasing problem.

Conventionally, some degree of anti-aliasing of Kirchhoff operators can be partially effected by a combination of trace interpolation, migration aperture control, operator dip filtering, and offset-dependent lowpass filtering (e.g., Gray, 1992). Trace interpolation decreases the spatial sample interval and thus increases the spatial Nyquist

[1]**email:** not available

frequency, but at the potentially prohibitive cost of increasing the total migration input load. Migration aperture control and operator dip filtering effectively represent ad hoc methods to suppress (aliased) steep dips contributions to the output image. Unfortunately, these steep dips may be precisely the events of interest when imaging salt flanks or vertical faulting. Source/receiver offset-dependent lowpass temporal filtering is an approximation to steep-dip operator anti-aliasing, but does not fully take into account the true time and dip variant nature of the problem, as exemplified by considering a simple zero offset (poststack) migration.

The outline of this paper is as follows. I first briefly review the anti-aliasing method by triangle filtering as proposed by Claerbout (1992). Next I discuss my implementation of the method and practical numerical aspects with regard to parallel computation on the SEP Connection Machine. Finally, I discuss an application of the method to a 3-D poststack data set from the Gulf of Mexico, and show that the anti-aliased Kirchhoff migration resolves steep dips on salt-sediment interfaces and faults better than a conventional aperture-weighted Kirchhoff migration.

ANTI-ALIASING THEORY

Claerbout (1992) proposed a method to anti-alias Kirchhoff space-time operators by local lowpass triangle filtering. Here, I extend Claerbout's anti-aliasing method to the Kirchhoff prestack time migration operator, which is given by:

$$t_k \;=\; t_s + t_r \;=\; \sqrt{\left(\frac{\rho_s}{v}\right)^2 + \tau^2} + \sqrt{\left(\frac{\rho_r}{v}\right)^2 + \tau^2}\;, \tag{1}$$

where t_k is the two-way Kirchhoff migration reflection traveltime, τ is the one-way vertical traveltime to the reflection point (pseudodepth) as shown in the geometry of Figure **??**, v is the rms migration velocity which may vary over (x, y, τ) in general, and ρ_s (ρ_r) is the distance measured along the planar recording surface between the source (receiver) and the vertical projection of the image point to the recording surface:

$$\rho_\star \;=\; \sqrt{(x_i - x_\star)^2 + (y_i - y_\star)^2}\;, \tag{2}$$

assuming the recording surface is horizontal at $z = \;constant$.

The spatial derivative of (1) is needed to determine the migration operator aliasing criterion:

$$\frac{\partial t_k}{\partial \rho} \;=\; +\sqrt{\left(\frac{\partial t_k}{\partial x_i}\right)^2 + \left(\frac{\partial t_k}{\partial y_i}\right)^2} \;\approx\; \frac{1}{v^2}\left(\frac{\rho_s}{t_s} + \frac{\rho_r}{t_r}\right) \;\approx\; \frac{\Delta t_k}{\Delta \rho}\;. \tag{3}$$

To remain unaliased, the temporal period T of any *local* waveform on a seismic trace at time t_k must be greater than $2\Delta t_k$:

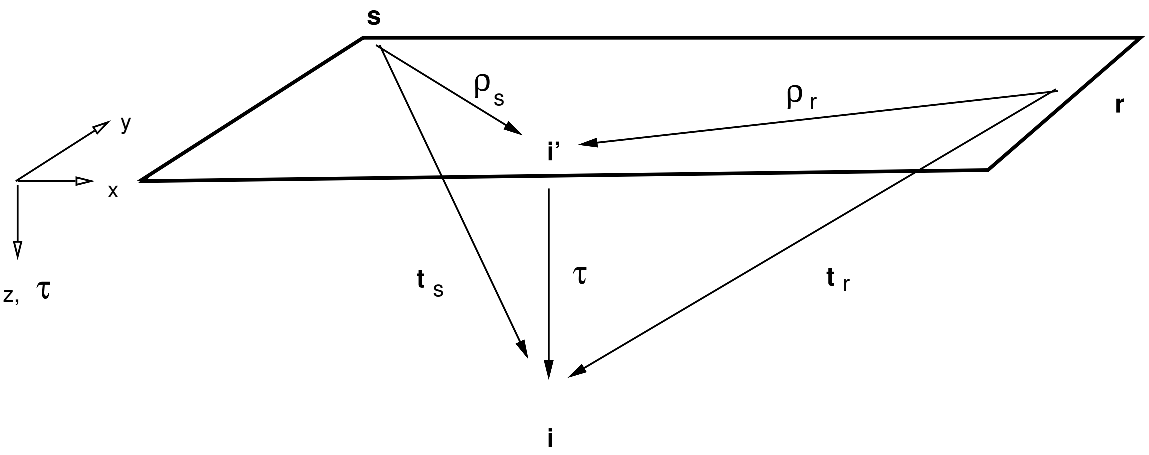

Figure 1: Geometry of the Kirchhoff 3-D prestack time migration operator for the anti-aliasing criterion. david1-geometry [NR]

$$T \;\geq\; 2\Delta t_k \;=\; 2\frac{\Delta\rho}{v^2}\left(\frac{\rho_s}{t_s}+\frac{\rho_r}{t_r}\right) \;. \tag{4}$$

I evaluate the effective rms spatial sampling interval $\Delta\rho$ for the prestack migration operator as

$$\Delta\rho \;\approx\; \sqrt{\frac{1}{2}\left(dx_s^2+dy_s^2+dx_r^2+dy_r^2\right)} \tag{5}$$

where I define $dx_\star$ and $dy_\star$ in the prestack case as

$$dx_\star \;=\; \frac{|x_i - x_\star|\Delta x}{\rho_\star} \tag{6}$$

and

$$dy_\star \;=\; \frac{|y_i - y_\star|\Delta y}{\rho_\star}\;. \tag{7}$$

Here, Δx and Δy are the true inline and crossline sampling intervals of the seismic trace data. For the poststack case, (3) reduces to

$$\frac{\Delta t_k}{\Delta\rho} \;\rightarrow\; \frac{4}{v^2}\left(\frac{\rho_m}{t_k}\right) \quad \text{(poststack)} \tag{8}$$

where ρ_m is the surface distance from the midpoint to the image point surface projection, and (5) reduces to

$$\Delta\rho \;\rightarrow\; \sqrt{dx_m^2 + dy_m^2} \quad \text{(poststack)} \tag{9}$$

where dx_m and dy_m are still validly defined by (6) and (7). Evidently,

$$\min\{\Delta x, \Delta y\} \;\leq\; \Delta\rho \;\leq\; \sqrt{(\Delta x)^2 + (\Delta y)^2}\,, \tag{10}$$

as expected. As an aside, the anti-aliasing criterion (4) may also be a good approximation for the case of Kirchhoff *depth* migration with the use of the rms migration velocity equivalent $v(x, y, \tau)$ to the depth migration interval velocity model $v_{int}(x, y, z)$.

The Kirchhoff migration operator anti-aliasing criterion (4) suggests an anti-aliasing method by local lowpass filtering of the input trace waveform in the vicinity of t_k. This local anti-alias lowpass filter is a function of trace time t_k and migration operator dip given by (3), in general. In particular, the anti-aliasing filter is not necessarily a simple function of offset or aperture. For example, a constant offset trace will be subject to relatively stronger lowpass filtering at early traveltimes t_s and t_r, compared to later arrival times (as expected by the greater relative curvature of a shallow versus deep migration impulse response).

I implement the local lowpass filters as triangular smoothing. Claerbout (1992) showed that for an arbitrary N-point triangle filter, the smoothing can be implemented efficiently by using only 3 filter coefficients instead of N, if the input trace data are first subjected to a sequential process of causal followed by acausal temporal integration. This observation offers a large savings in computational effort when applying the triangle filters. I relate an N-point triangle to the aliasing period T by the relation $T = 2(N + 1)\Delta t$, where Δt is the true temporal trace sample interval. My chosen anti-aliasing criterion (4) in terms of triangle filter length N becomes:

$$N \;\geq\; \max\left(\frac{\Delta\rho}{v^2\Delta t}\left(\frac{\rho_s}{t_s} + \frac{\rho_r}{t_r}\right) - 1,\;\; 1 \right)\;. \tag{11}$$

For poststack geometries, this result reduces to:

$$N \;\geq\; \max\left(\frac{4\rho_m\Delta\rho}{v^2 t_k \Delta t} - 1,\;\; 1 \right) \quad \text{(poststack)}\;\;. \tag{12}$$

PRACTICAL IMPLEMENTATION

Parallel processing

The Kirchhoff 3-D migration algorithm I wrote for both the conventional and anti-aliased migrations in this study are implemented on a 32-node parallel processing

Connection Machine (CM5). The algorithm is similar in structure to that of Lumley and Biondi (1991), except for some modifications to take advantage of vector unit processing, streamlining for this poststack case, and extensions to incorporate the anti-aliasing option with local triangular filtering.

To take advantage of parallelism, a large cube of input trace data is loaded and aligned in-processor with the output migrated image cube. Then the traces are migrated in parallel into the image volume, with serial loops running over pseudodepth τ, and circular processor-to-processor data shifts using the CM Fortran 90 intrinsic `cshift`. The conventional algorithm runs at a total average sustained rate of about 500 Mflop/s, and the anti-aliased version runs at about 350 Mflop/s. These figures include all i/o and frequent saving to disk of partial migration results (my own ad hoc checkpoint restart solution). The migration currently processes 30,000 poststack input traces into an output cube of dimensions 300x100x512 in about 20 CPU hours for the conventional migration method, compared to a total of about 30 CPU hours for the anti-aliased migration method.

Triangles in parallel

This parallel processing data flow poses some unique problems to anti-aliasing compared to more convention trace-sequential scalar or vector processing strategies. In a trace-sequential migration, several copies of a single input trace can be filtered at different high-cut frequencies and then used appropriately during anti-aliasing depending on the local migration operator dip. In a parallel data flow, I cannot afford to keep an extra copy of my input data in memory, since it is as large as my output image volume, and nearly half the total available memory in order to optimize parallelism in the computations. I have experimented with a more conservative memory-use algorithm structure for the input data, but the underlying principle of not easily maintaining multiple copies of input data in memory remains the same.

Fortunately, the local triangle lowpass filtering approach to anti-aliasing can be done on the fly without storing multiple copies of input data. All the input traces are first given a full 3-D time derivative (as opposed to the half-time derivative of 2-D migration), and then integrated once causally, and once acausally. Each process is implemented in parallel over the surface coordinate direction, each trace residing serially in-processor. The triangle filtering for any triangle length N is then just a 3-point filter operation on the doubly integrated traces [see Claerbout (1992)], which is also implemented in parallel over all input traces.

Indirect memory addressing

The parallel migration tends to be bound in the inner loop by indirect memory addressing for the trace sample values at the migration operator times t_k. Simple linear interpolation of a trace value for the time t_k requires two indirect memory accesses, any single nearest-neighbor triangle interpolation requires three indirect memory accesses (the triangle peak is placed at the nearest neighbor location of t_k), and a general triangle interpolation for filter coefficients falling on non-sampled time locations requires six indirect memory accesses. I use the nearest-neighbor triangle anti-aliasing scheme since it is only 1.5x slower than simple linear interpolation, instead of the general triangle interpolation method which is a rather unacceptable 3x more inefficient than simple linear interpolation. The drawback to the nearest-neighbor triangle filters is that more smoothing is done than required in unaliased regimes where linear interpolation would have sufficed. Since the traces have been doubly integrated, and I can't afford to keep a copy of non-integrated input traces, nor switch to the 6-point general triangle filters easily in a SIMD algorithm flow, I have elected to always smooth at a minimum of three adjacent points on the time access. This is fine for data that has energy mostly below half-Nyquist, but may represent over-smoothing and unnecessary loss of some bandwidth otherwise.

Triangle length and scaling

To take advantage of the efficiency of the nearest-neighbor triangle interpolation in terms of minimizing indirect memory addressing, I use a minimum triangle length such that $N \geq 3$. Above, I discussed the danger of over-smoothing resulting from this choice. I also limit the maximum triangle length such that $N \leq (2f_{min})^{-1}$, where f_{min} is a user-specified parameter indicating the minimum frequency at which real signal is present. This prevents the lowpass anti-aliasing filters from enhancing low-frequency noise (and even d.c.) that may be present in the data, and/or boosted by the double trace integration process. Additionally, to preserve the relative amplitude of a low-frequency anti-aliased reflection compared to a fullband unaliased reflection, I scale the triangles by inverse height instead of the usual inverse area factor. This boosts the peak amplitudes of lowpassed steep dip events to compensate for their loss of bandwidth due to the anti-aliasing process. This inverse height triangle scaling is a first order amplitude effect on the migration impulse responses, and warrants future study. Finally, I weight the anti-aliased migration operator with the conventional migration aperture and $\cos^n \theta$ obliquity factors to suppress post-vertical (evanescent) time-migration impulse response energy.

DATA EXAMPLE

The algorithm implemented to perform the Kirchhoff migration operator anti-aliasing based on equations (1) – (11) is coded in parallel Fortran 90, and tested on the Stanford Exploration Project's 32-node Connection Machine (CM5).

Seismic data

The marine data are a 3-D DMO'ed poststack data volume acquired over a salt intrusion in the Gulf of Mexico, donated by Halliburton Geophysical Services to SEP. The test data set used here is a smaller portion of the complete data set. I am using 30,000 poststack traces binned on a 300x100 surface grid, with a decimated inline (300) spacing of 37.5 m and an original crossline (100) spacing of 25 m, representing a surface area of 11 km inline by 2.5 km crossline. The traces were decimated to 8 ms to save memory, without loss of signal bandwidth.

Figures **??** and **??** show a crossline and inline section respectively, sliced from near the center of the input stacked data volume. The crossline section shows a sedimentary anticline over some rough diffractions related to salt. The inline section shows fairly gently dipping sediments abutting a region of steep dip diffractions and reflections associated with salt-sediment interfaces.

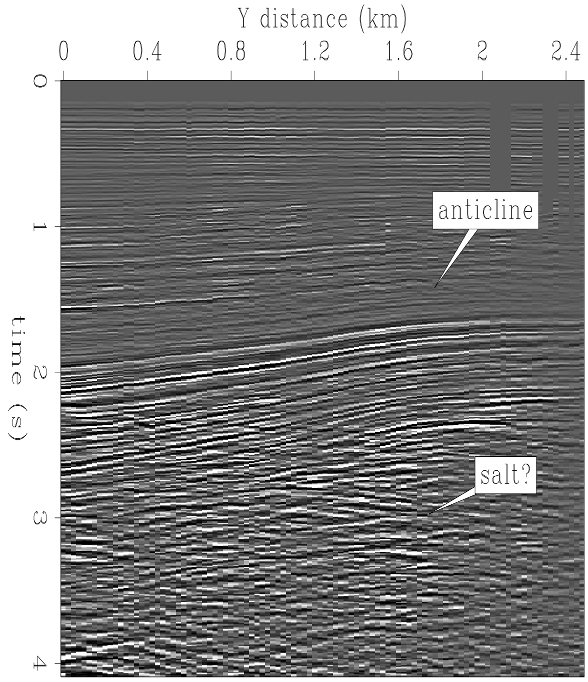

Figure 2: Crossline section from near the center of the input stacked data volume. Notice the sedimentary anticlinal structure uplifted by the underlying salt (rough diffraction region). david1-ysection-ann [CR]

Impulse responses

Figure **??** shows the effective migration operator "impulse responses" to standard and anti-aliased migrations. The responses are the result of migrating 10 adjacent traces with the two different methods to examine the effects of migration operator spatial aliasing. The "standard" response incorporates the effect of a $\cos^2 \theta$ obliquity

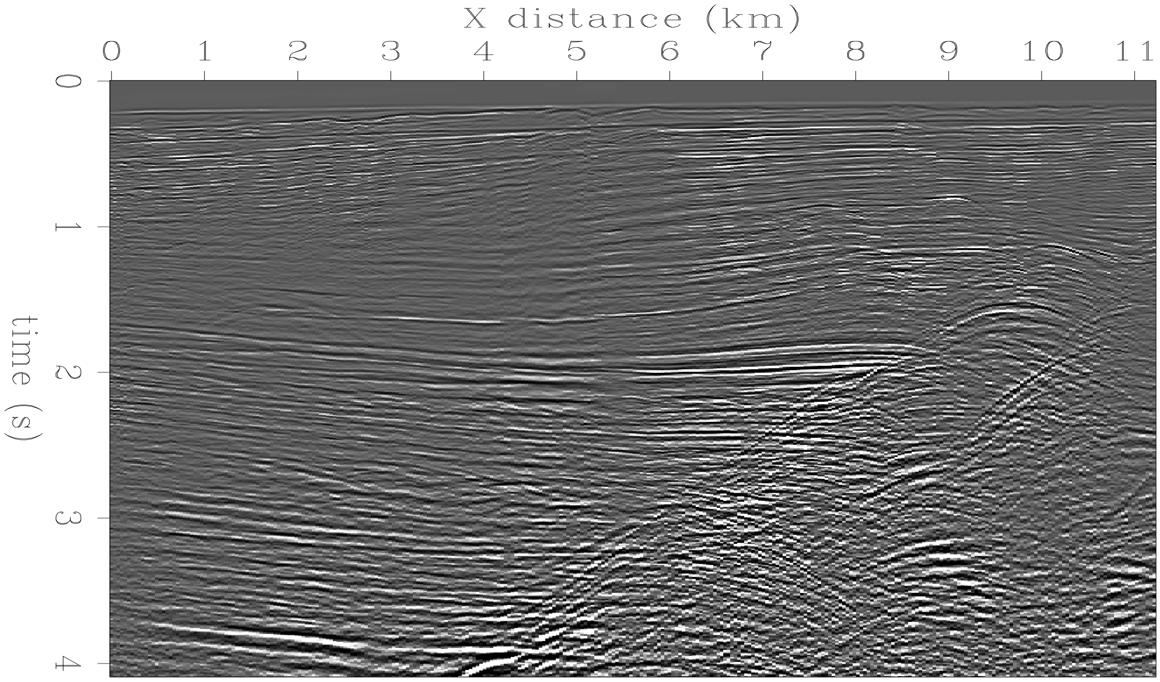

Figure 3: Inline section from near the center of the input stacked data volume. The strong diffraction and steep-dip reflection energy is associated with salt-sediment interfaces. Some weak evidence of shallow faulting is seen at 8 km distance at 1.5 seconds. david1-xsection [CR]

dip filter and a 45 degree migration aperture weighting to partially combat spatial aliasing. This eliminates near-vertical steep dip aliasing, but leaves a fair amount of spatially aliased speckling within the aperture cone. The "anti-aliased" response combines the standard response with the local lowpass anti-aliasing triangle filtering, including the inverse triangle height weighting. Note that most of the aliasing has been suppressed, resulting in smooth and coherent migration ellipses. At steep dips the anti-aliased operator is of lower frequency in comparison to the standard response, as anticipated, but of similar bandwidth near the horizontal (zero-dip) portions of the operator.

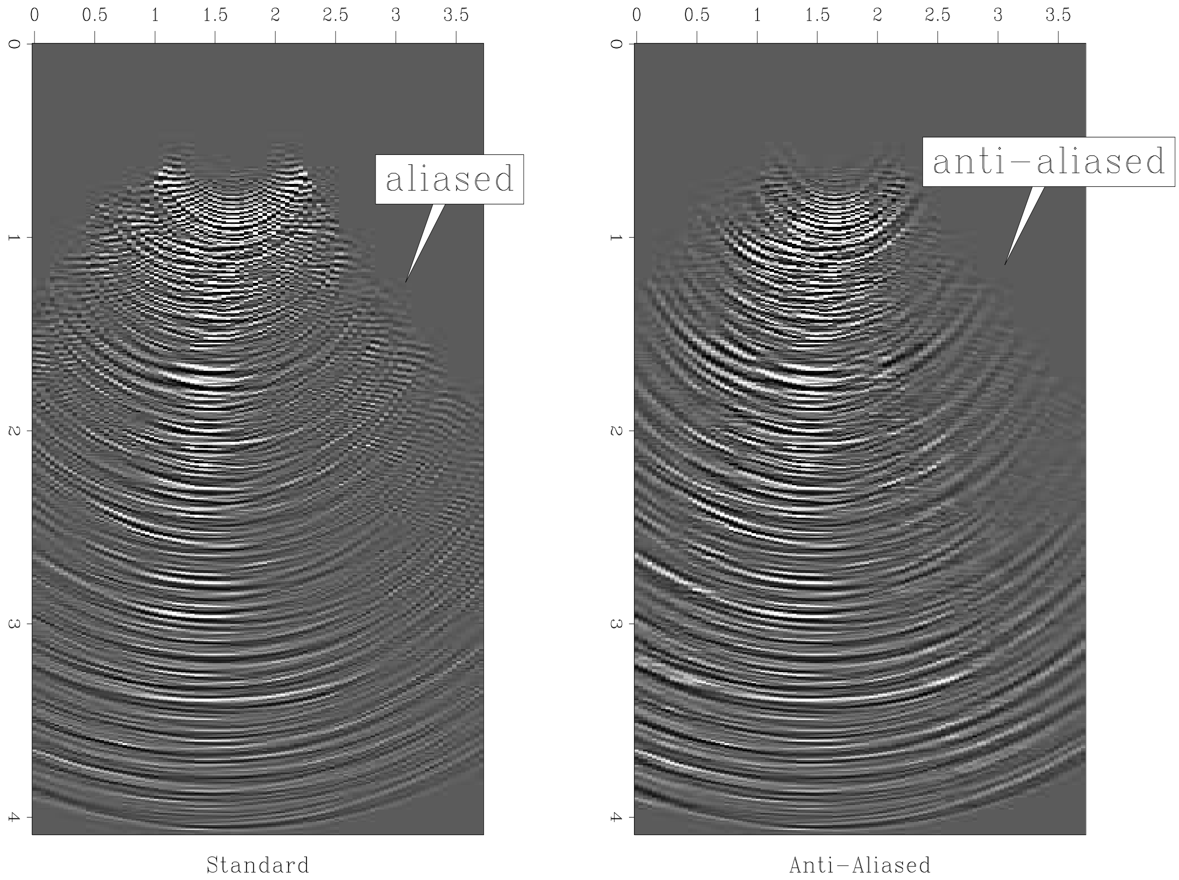

Figure 4: Effective migration operator "impulse responses" to standard, and anti-aliased migrations. The "standard" response has a $\cos^2\theta$ dip filter and a 45 degree aperture weighting cone. The anti-aliased response is identical to the standard response except that it also has the anti-aliasing triangle filters applied. david1-responses-ann [CR]

3-D Migrations

I ran standard and anti-aliased Kirchhoff 3-D poststack time migrations on the Halliburton data subset. The standard migration corresponds to the left impulse response of Figure **??**, i.e., a 45 degree aperture and $\cos^2\theta$ obliquity dip-filtering. The anti-aliased migration corresponds to the right impulse response of Figure **??**, which has the additional anti-aliasing local triangle filtering applied as described previously. The migrations take approximately 20 CPU hours per run for the standard migration, and 30 CPU hours for the anti-aliased migration, on the SEP 32-node CM5. In this section, I will briefly compare the migrated images obtained by both methods.

Figure **??** shows inline sections sliced from the standard (upper) and anti-aliased (lower) migration volumes, at a constant $y = 0.225$ km. Aliasing of the type shown in the left panel of Figure **??** has severely contaminated the upper migration image. Even the horizontal structure has been degraded by steep dip spatial aliasing of the migration operator. The anti-aliased migration (lower) is much more coherent in terms of horizontal structure, and possibly images two salt-sediment interfaces. Also, the anti-aliased image clearly shows shallow faulting above the interpreted salt location, including a slightly clockwise-rotated fault block at 9.5 km and 1.5 seconds.

Figure **??** shows inline sections sliced from the standard (upper) and anti-aliased (lower) migration volumes, at a constant $y = 0.875$ km. Again, the anti-aliased image is much more coherent in all aspects, although visually a little more low-frequency in content. The third inline section of Figure **??** is at a constant $y = 2.300$ km. Here, the anti-aliased image clearly shows the salt peak, as well as the intersection between the salt and anticlinal sediments where the salt appears to have pierced through. Also, some near vertical faulting is apparent directly above the salt peak at the 8 and 9 km locations. These features are barely visible in the standard migration, and would be much more challenging to interpret without the aid of the anti-aliased image.

Figure **??** shows a crossline section sliced from each migrated volume at a constant $x = 7.1625$ km location. Note the coherent resolution of the anticlinal sediment structure in the anti-aliased migration (right panel). With a little imagination, we might be seeing the top of salt which underlays the sediment package at 2.5 seconds, and the fuzzy bottom of the salt intrusion at 3.0 seconds. Below the interpreted top of salt, a depth migration with salt and sediment velocity specification is probably required to focus the deeper reflection events.

Figure **??** shows a time slice from each of the standard (upper) and anti-aliased (lower) migration volumes, at a constant $\tau = 0.128$ seconds. The anti-aliased time slice shows a 3 km long continuous radial fault associated with the salt intrusion. Since these time slices are essentially at the surface, the salt approximately lies between and underneath the two pseudo-parallel radial faults, and the salt peak penetrates the sediment anticline beneath the lower right corner of the plot. The anti-aliased migration image clearly shows this fault continuity and the fact that it penetrates through to the surface, in comparison to the more ambiguous result from the standard migration time slice in the upper panel.

Figure **??** shows a time slice from each of the standard (upper) and anti-aliased (lower) migration volumes, at a constant $\tau = 1.752$ seconds. In the anti-aliased image, the salt peak has clearly penetrated the anticlinal sediment structure in the lower right corner of the plot. A radial fault (salt-filled?) is barely discernible, but definitely seems to curve into the major discontinuity in folded sediments at $\{x, y\} = \{8.5, 1.7\}$ km. The second radial fault is not well imaged at this pseudodepth. Note the contrast between the coherency of the upper and lower panels.

Figure **??** shows time slices at a constant $\tau = 1.880$ seconds. In the anti-aliased migration image, both radial faults seem to be clearly imaged, but almost absent from the standard migration panel. The fault reflections are fairly strong amplitude, perhaps indicating they are salt-filled. The two faults bound a fault block which contains reflectors that dip steeply and acutely into the plane of the page, especially at $x = 9.5$ km in the $y = 1.5$ km range. In contrast, the anticlinal sediment structure to the left dips more within the horizontal plane of the page.

CONCLUSIONS

I implemented an anti-aliasing method for Kirchhoff migration operators, based on local triangle filtering. The N-point triangles are efficiently applied as 3-point filters after causal and acausal integration of the seismic trace data. This method is well suited for parallel processing algorithms, where storage of multiple copies of various high-cut filtered versions of the input data is not often practical. I compare the anti-aliasing method to a standard Kirchhoff 3-D migration, using a salt intrusion data set from the Gulf of Mexico. Preliminary results indicate that careful anti-aliasing can enhance steep-dip reflections from faults and salt-sediment interfaces during the process of 3-D seismic migration imaging.

ACKNOWLEDGMENTS

This work benefitted from anti-aliasing discussions I had with Jon Claerbout, Francis Muir, Dave Nichols and Dimitri Bevc. Dimitri and Jon helped improve the paper with their thorough proofreading. Halliburton Geophysical Services kindly donated the 3-D salt intrusion data used in this example, and Mihai Popovici volunteered to unload the data from 6250 tapes to disk.

REFERENCES

Claerbout, J. F., 1992, Anti aliasing: Stanford Expl. Proj. Report, **73**, 371–389.

Gray, S. H., 1992, Frequency-selective design of the Kirchhoff migration operator: Geophysical Prospecting, **40**, 565–571.

Lumley, D. E., and Biondi, B., 1991, Kirchhoff 3-D prestack time migration on the Connection Machine: Stanford Expl. Proj. Report, **72**, 123–134.

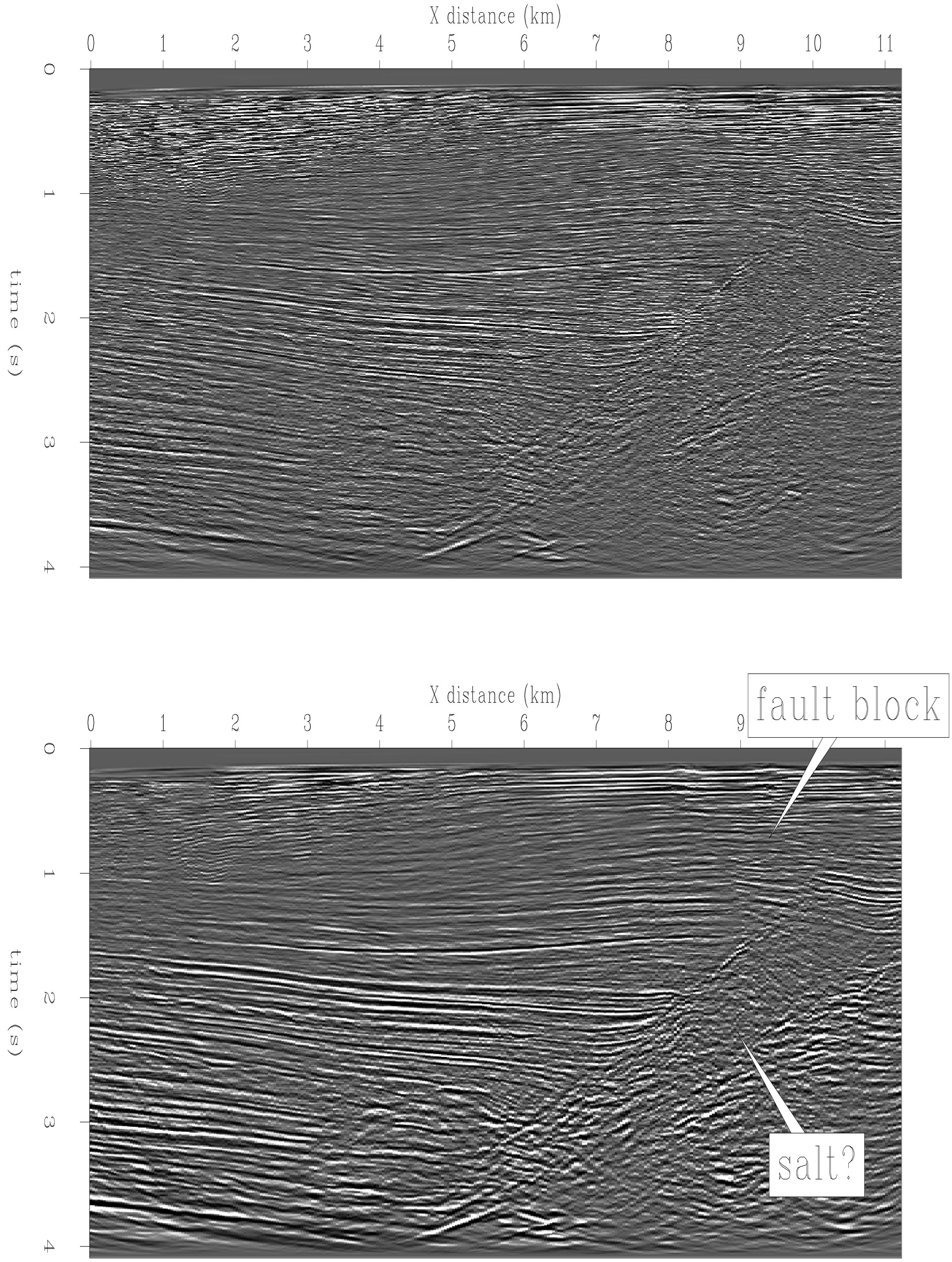

Figure 5: Inline sections sliced from the standard (upper) and anti-aliased (lower) migration volumes, at a constant $y = 0.225$ km. The anti-aliased migration is much more coherent in terms of horizontal structure, a possible salt-sediment interface or two, and shallow faulting above the interpreted salt location, including a slightly clockwise-rotated fault block at 9.5 km and 1.5 seconds. david1-x9-ann [CR]

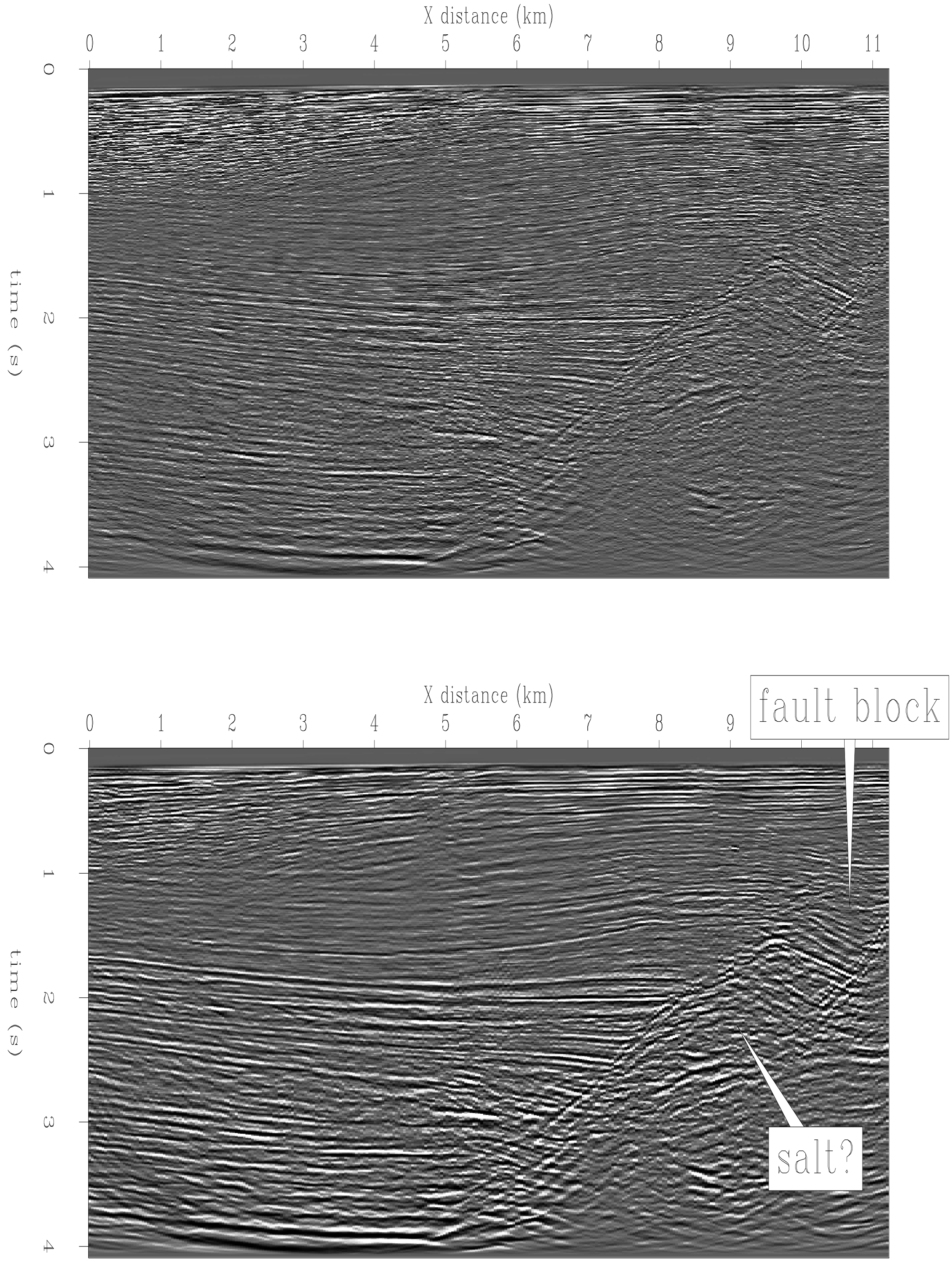

Figure 6: Inline sections sliced from the standard (upper) and anti-aliased (lower) migration volumes, at a constant $y = 0.875$ km. Again, the anti-aliased migration is much more coherent, although of notably lower frequency content. Note the strong salt-sediment interfaces/faults, and the strongly clockwise-rotated fault block at 10.5 km and 1.5 seconds. $\boxed{\text{david1-x35-ann}}$ [CR]

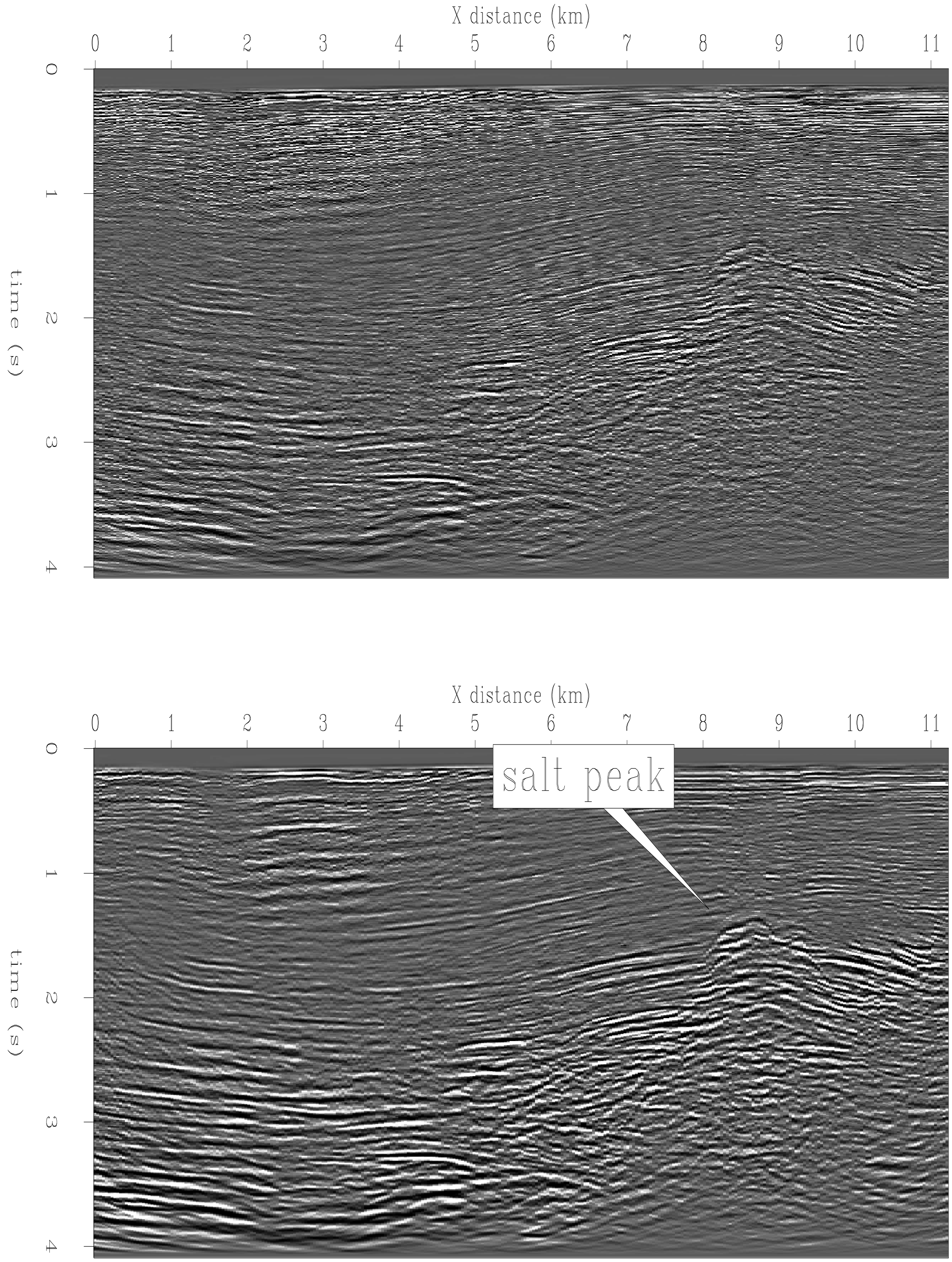

Figure 7: Inline sections sliced from the standard (upper) and anti-aliased (lower) migration volumes, at a constant y = 2.300 km. A salt peak is clearly visible at 8.5 km and 1.5 seconds in the anti-aliased image. This interpretation would be much more challenging given only the standard image in the upper panel. david1-x92-ann [CR]

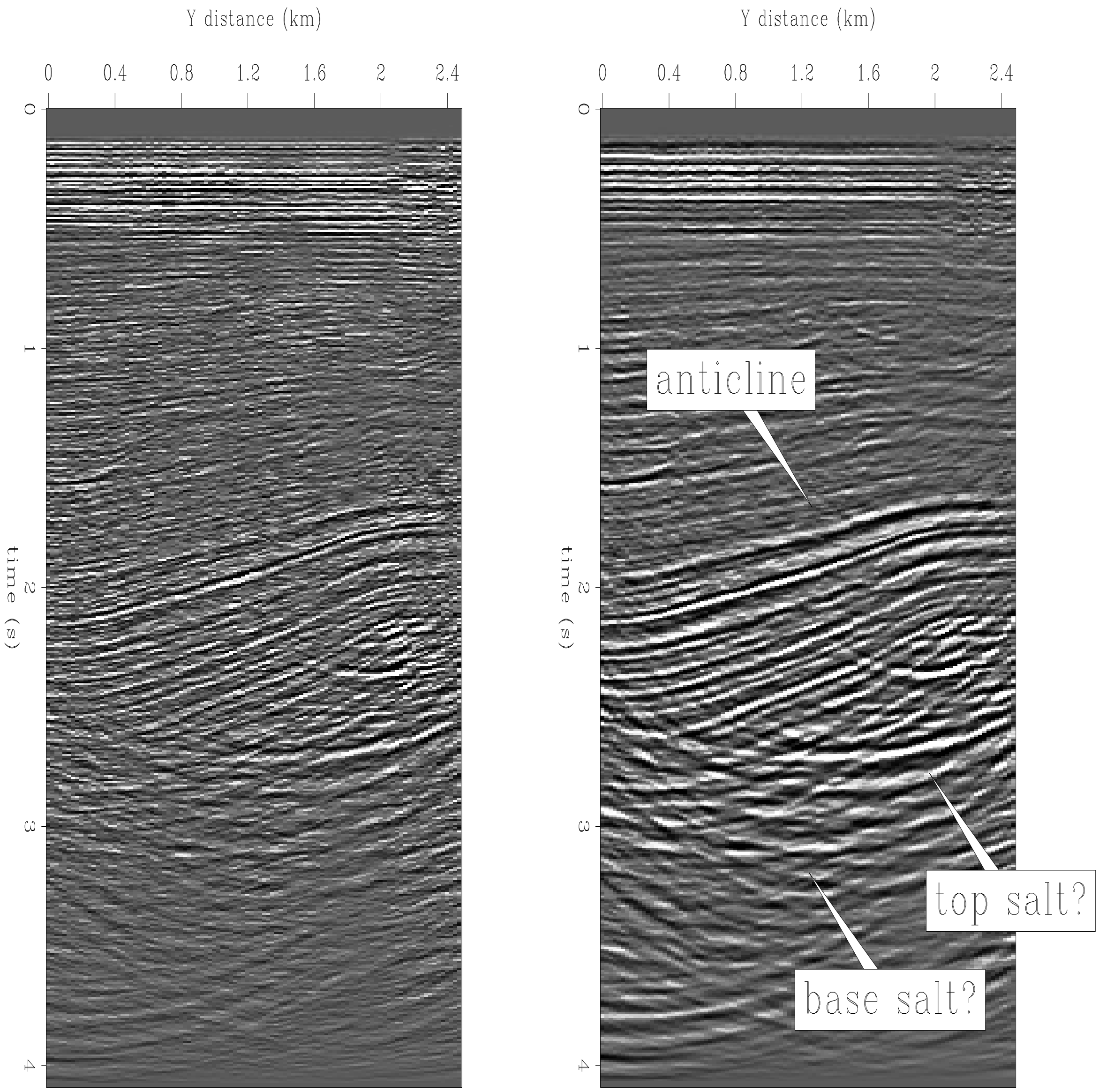

Figure 8: Crossline sections sliced from the standard (left) and anti-aliased (right) migration volumes, at a constant $x = 7.163$ km. Note the coherent resolution of the anticlinal sediment structure in the anti-aliased migration panel. With a little imagination, we might be seeing the top of salt which underlays the sediment package at 2.5 seconds, and the fuzzy bottom of the salt lens intrusion at 3.0 seconds. david1-y191-ann [CR]

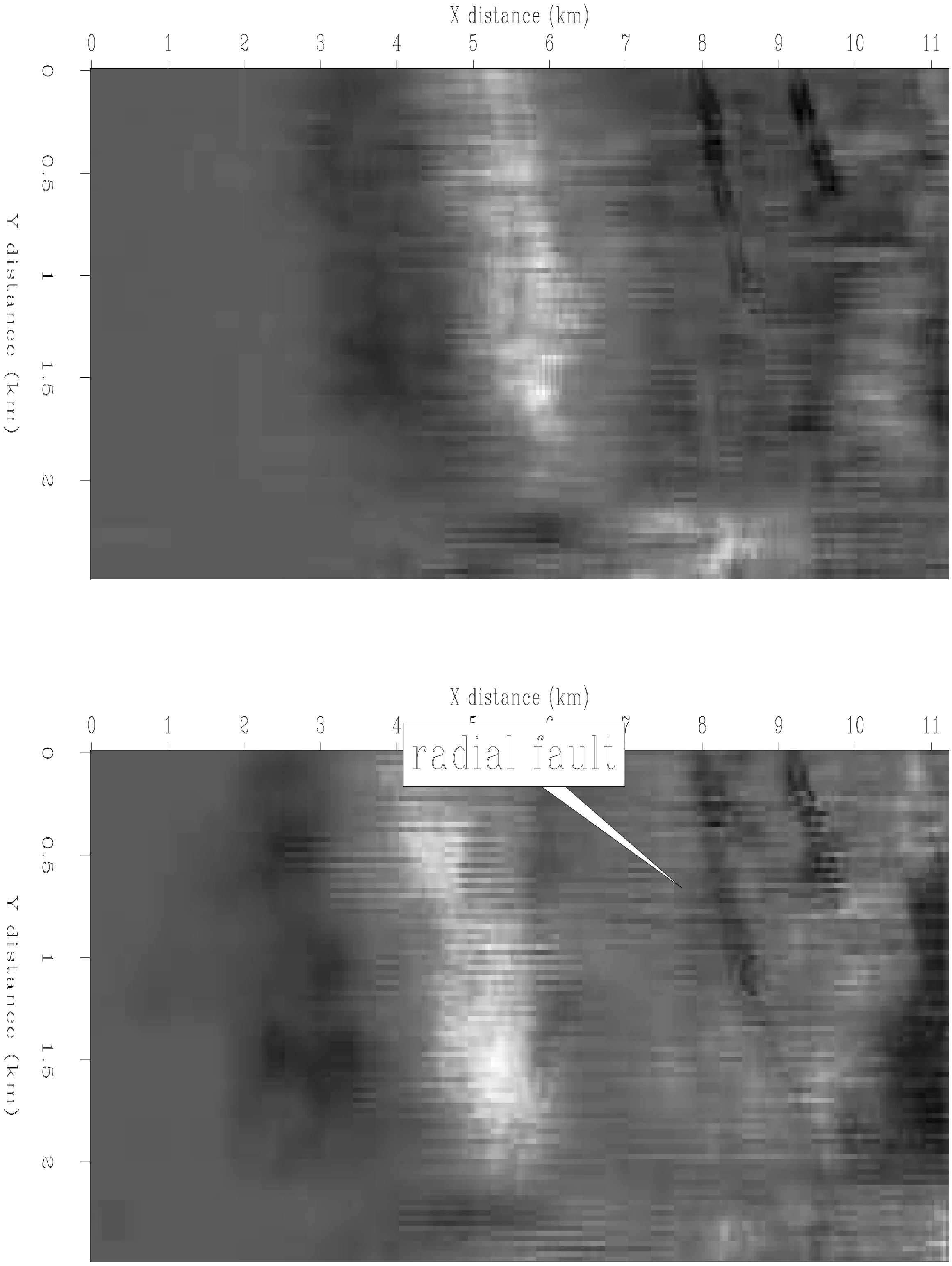

Figure 9: Time slices cut from each of the standard (upper) and anti-aliased (lower) migration volumes, at a constant $\tau = 0.128$ seconds. The anti-aliased time slice shows a continuous 3.0 km long radial fault associated with the salt intrusion. david1-z16-ann [CR]

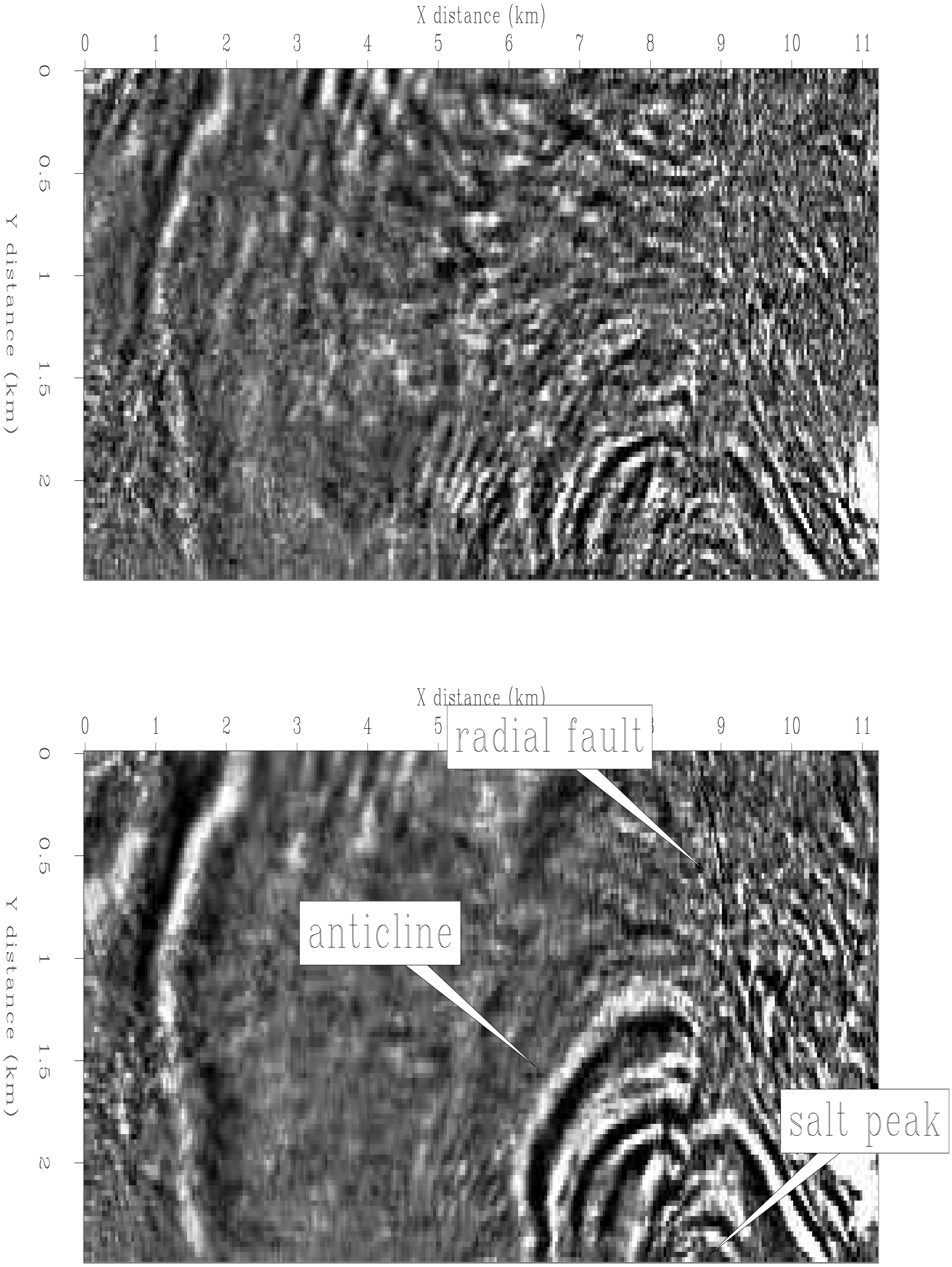

Figure 10: Time slices cut from each of the standard (upper) and anti-aliased (lower) migration volumes, at a constant $\tau = 1.752$ seconds. The salt peak has clearly penetrated the anticlinal sediment structure in the lower right corner of the plot. A radial fault (salt-filled?) is barely discernible, but definitely seems to curve into the major discontinuity in folded sediments at $\{x, y\} = \{8.5, 1.7\}$ km. david1-z219-ann [CR]

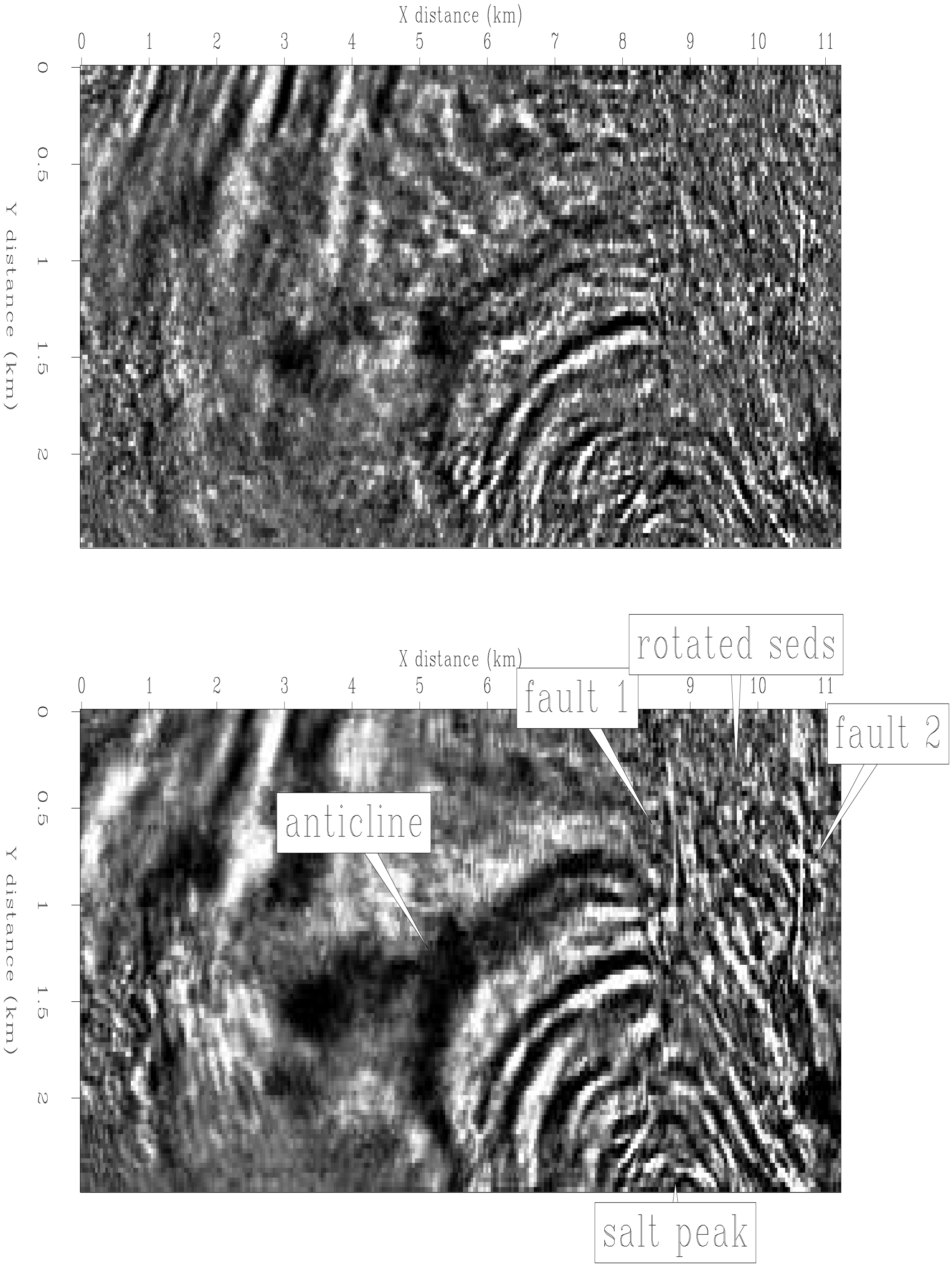

Figure 11: Time slices cut from each of the standard (upper) and anti-aliased (lower) migration volumes, at a constant $\tau = 1.880$ seconds. Two radial faults are clearly imaged, which bound a fault block containing reflectors that dip steeply and acutely into the plane of the page, especially at $x = 9.5$ km in the $y = 1.5$ km range. In contrast, the anticlinal sediment structure to the left dips more within the horizontal plane of the page. david1-z235-ann [CR]